A robotic fish caudal fin: effects of stiffness and motor program on locomotor performance

The Journal of Experimental Biology 215, 56-67

doi:10.1242/jeb.062711

RESEARCH ARTICLE

A robotic fish caudal fin: effects of stiffness and motor program on locomotor performance

Christopher J. Esposito[1], James L. Tangorra[2,*], Brooke E. Flammang[3] and George V. Lauder[3]

[1]Electric Boat, General Dynamics, Groton, CT 06430, USA, [2]Department of Mechanical Engineering, Drexel University, Philadelphia, PA 19104, USA and [3]Museum of Comparative Zoology, Harvard University, Cambridge, MA 02138, USA

*Author for correspondence (tangorra@coe.drexel.edu)

Accepted 5 October 2011

SUMMARY

We designed a robotic fish caudal fin with six individually moveable fin rays based on the tail of the bluegill sunfish, *Lepomis macrochirus*. Previous fish robotic tail designs have loosely resembled the caudal fin of fishes, but have not incorporated key biomechanical components such as fin rays that can be controlled to generate complex tail conformations and motion programs similar to those seen in the locomotor repertoire of live fishes. We used this robotic caudal fin to test for the effects of fin ray stiffness, frequency and motion program on the generation of thrust and lift forces. Five different sets of fin rays were constructed to be from 150 to 2000 times the stiffness of biological fin rays, appropriately scaled for the robotic caudal fin, which had linear dimensions approximately four times larger than those of adult bluegill sunfish. Five caudal fin motion programs were identified as kinematic features of swimming behaviors in live bluegill sunfish, and were used to program the kinematic repertoire: flat movement of the entire fin, cupping of the fin, W-shaped fin motion, fin undulation and rolling movements. The robotic fin was flapped at frequencies ranging from 0.5 to 2.4 Hz. All fin motions produced force in the thrust direction, and the cupping motion produced the most thrust in almost all cases. Only the undulatory motion produced lift force of similar magnitude to the thrust force. More compliant fin rays produced lower peak magnitude forces than the stiffer fin rays at the same frequency. Thrust and lift forces increased with increasing flapping frequency; thrust was maximized by the 500× stiffness fin rays and lift was maximized by the 1000× stiffness fin rays.

Supplementary material available online at http://jeb.biologists.org/cgi/content/full/215/1/56/DC1

Key words: fish, caudal fin, fin ray, robotics, biomimetics, flexibility, locomotion.

INTRODUCTION

The caudal fin of fishes has often been viewed by engineers as a relatively simple propulsive surface that is flapped by fish in a two-dimensional motion that is an extension of the undulatory wave generated by myotomal body musculature (Barrett et al., 1999; Alvarado and Youcef-Toumi, 2006; Anton et al., 2009). However, in many fishes the caudal fin is used not exclusively for thrust production, but also to create forces and moments that control the orientation of the fish *via* complex conformational changes and motion programs (Lauder, 1982; Drucker and Lauder, 1999; Lauder, 2000; Lauder and Drucker, 2004; Flammang and Lauder, 2008; Tytell et al., 2008; Flammang and Lauder, 2009). These shape changes and kinematic patterns are produced by fin rays within the caudal fin that are moved by intrinsic caudal musculature that is distinct from the segmented body muscles (Lauder, 2006; Flammang and Lauder, 2008; Flammang and Lauder, 2009). Bony fish such as bluegill sunfish (*Lepomis macrochirus*) are thus able to actively deform the surface of their fins through individual fin ray motions and/or by altering the stiffness of individual fin rays (Alben et al., 2007; Flammang and Lauder, 2008; Lauder et al., 2011a; Lauder et al., 2011b).

The caudal fin of bony fish such as the bluegill sunfish has been demonstrated to generate locomotor forces in the lateral, lift and thrust directions, indicating that the tail is being used for more than just propulsion (Lauder and Madden, 2006; Lauder and Madden, 2007; Flammang et al., 2011). Fish are capable of altering the relative magnitudes of these forces and to vector water momentum in appropriate directions to execute maneuvers; this ability is a function of the design of the caudal fin with its individually controllable fin rays.

Historically, fish-inspired robots that have modeled the caudal fin have used a rigid or moderately flexible flat surface that is actuated about a single axis in an undulatory or flapping motion from the caudal peduncle area (where the body narrows and transitions to the tail). Studies like these have used the caudal fin to create forward propulsion and to control simple turning maneuvers by biasing the flapping of the fin to one side of the robot. This approach has proven useful for a number of fish-inspired robotic designs (Barrett et al., 1999; Alvarado and Youcef-Toumi, 2006; Long et al., 2006; Zhang et al., 2008; Anton et al., 2009; Long et al., 2010; Low and Chong, 2010). However, a two-dimensional flat-plate-like representation of the three-dimensional (3-D) fin motion without the ability to actively control tail conformation means that it is difficult for current robotic designs to control the direction and magnitude of the force vector. Recent computational studies, such as those by Zhu and Shoele (Zhu and Shoele, 2008; Shoele and Zhu, 2009), have begun to address the role of fin rays, ray stiffness and fin conformational changes on force production, but there are no experimental data from caudal fin robotic devices that allow the evaluation of key parameters such as stiffness, motion program and frequency on locomotor force production.

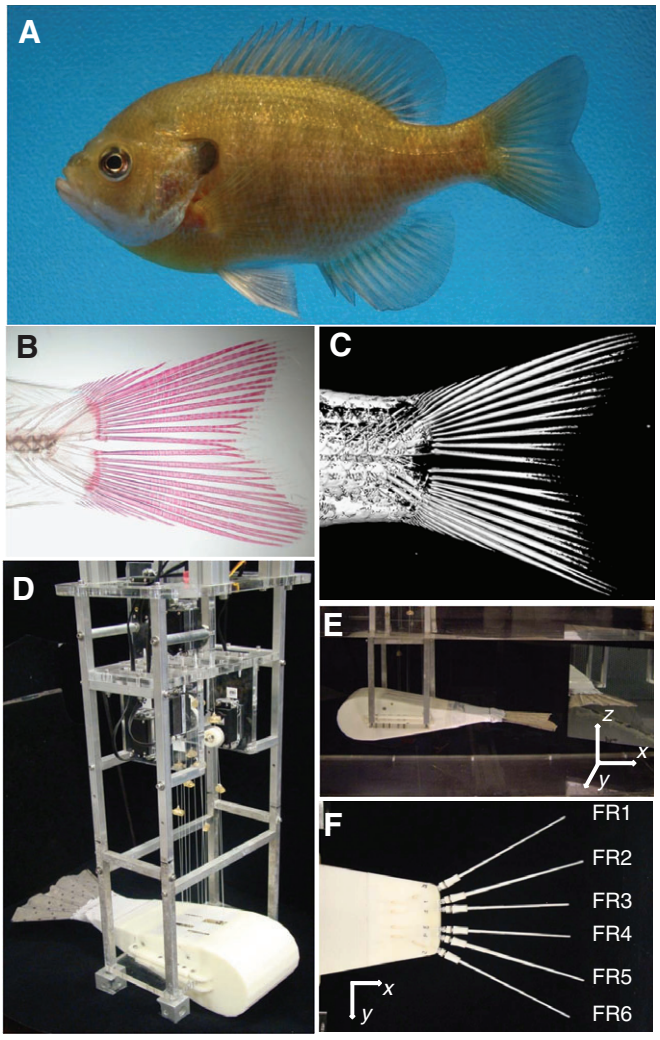

Fig. 1. Overview of the biomimetic design of the robotic fish caudal fin. (A) Bluegill sunfish, *Lepomis macrochirus*, the biological model for this robotic device. (B) Cleared-and-stained and (C) computed microtomography scan of the sunfish tail region. Bones are stained red in B. (D) Overview of the caudal fin robot held on a stand in the laboratory. The frame houses the rotational servomotors, controller board and attachment mechanisms for the carriage system. The low-stretch string tendons, attached to the servomotor horns, are guided through the body to the fin rays. (E) View of the caudal fin robot shown in the flow tank where experiments were conducted. The low-friction air carriage on which the robotic device is mounted is out of view at the top. (F) View of the caudal fin robot with six fin rays protruding from the peduncle of the robot. The fin rays are labeled 1 through 6, with 1 considered by our convention the dorsal-most fin ray, and 6 the ventral-most fin ray. The webbing and tendons are removed to show the peduncle area and fin ray attachment mechanism. The biorobotic fin was oriented in the horizontal plane to facilitate experimentation. Lift forces were therefore measured in the horizontal plane (corresponding to the dorsoventral axis of a fish, in the *y*-axis orientation) and thrust forces were measured along the rostrocaudal axis of the fish (along the *x*-axis).

The goal of this paper is to contribute to our understanding of fish caudal fin function by constructing a robotic model with six individually controllable fin rays that allows detailed control over the movement pattern of the fin. The robotic caudal fin was programmed to move in five distinct patterns based on caudal fin kinematics measured in our previous work on freely swimming bluegill sunfish (Flammang and Lauder, 2008; Flammang and Lauder, 2009). The caudal fin robot was then used to investigate the effect of changing fin ray stiffness, flapping frequency and kinematic pattern on locomotor performance as measured by patterns of thrust and lift produced during the tail flapping cycle.

MATERIALS AND METHODS

Design of the caudal fin robot

A six fin-rayed robotic caudal fin was developed using information obtained from biological studies of the bluegill sunfish caudal fin (Fig. 1) (Lauder, 1982; Lauder, 2000; Lauder and Drucker, 2004; Flammang and Lauder, 2008). This design process was similar to that used for the robotic pectoral fin by developed in Tangorra et al. (Tangorra et al., 2007; Tangorra et al., 2010). The robotic caudal fin model was scaled to have linear dimensions approximately four times larger than an adult bluegill sunfish of 20 cm total length. The 19 fin rays of the biological caudal fin were modeled using six engineered fin rays. This was the minimum number of rays required to satisfactorily execute the desired kinematic patterns, and allow independent control of the dorsal and ventral tail lobes. This fin ray number was also sought to limit the complexity of the design and to help reduce the potential for failure. Each of the robotic fin rays were individually actuated by a rotational servomotor (HS-645MG, Hitec RCD, Poway, CA, USA) *via* low-stretch polyethylene tendons attached to the base of the fin ray. The compliant webbing material covering the fin rays was a blend of polyester (82%) and elastane (18%) (Under Armour, Inc., Baltimore, MD, USA), which was coated with a thin layer of latex to decrease fluid diffusion and to stiffen the material slightly (Fig. 2A). The body supporting the robotic caudal fin tapers smoothly toward the caudal peduncle (Fig. 1D,E) to reduce total drag and minimize the turbulent effects of any protuberances that could alter water flow over the robotic tail. The region of the caudal peduncle was covered with a cloth sleeve (Fig. 2A) that served to smooth this transition area and cover the fin ray bases. Tendons to control the fin rays emerged from slots at the posterior end of the body (Fig. 2B) and were attached to each side of the fin ray bases (Fig. 2C). The fin ray bases allowed fin rays of different stiffness to be attached without altering the tendon tension. Tensioning of the individual fin ray tendons was an important step in setting up the robotic caudal fin, and setting the correct tendon tension proved important in being able to produce the desired motion. To aid in this process, small tensioners were custom designed (Fig. 2D) and were located above the water level to allow individual tendons to be tightened or loosened as needed. Tendons from the servomotors located above the water entered the body through slots, and made a 90 deg turn inside the body around low-friction blocks (Fig. 2E) to emerge at the base of each fin ray.

Kinematics

Five movement patterns derived from three-dimensional kinematic data and high-speed video of the caudal fin of bluegill sunfish during steady swimming and maneuvering, from previous studies by Flammang and Lauder (Flammang and Lauder, 2008; Flammang and Lauder, 2009), were selected to be programmed into the robotic model. For ease of communication in this paper, these five motion programs are labeled as flat (supplementary material Movie 2), cupping (supplementary material Movie 3), W, undulation (supplementary material Movie 4) and rolling (supplementary material Movie 5) (Fig. 3).

Our baseline motion program is designated as the flat motion program in which all fin ray bases were moved synchronously through a tail beat with angular excursions (Fig. 3, flat motion) so that all caudal fin rays moved together. Even though fluid loading

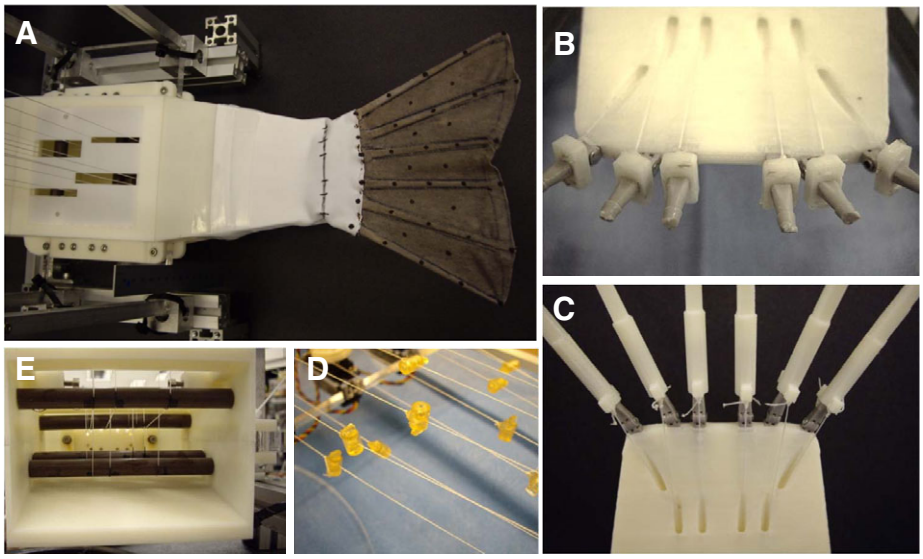

Fig. 2. Specific features of the design of the robotic fish caudal fin. (A) View from above to show the low-stretch polyethylene fin ray tendons entering through slots in the body, the cloth boot that streamlines the caudal peduncle area with the transition to the fin ray bases, and the caudal fin (with black dots added for ease of 3-D kinematic tracking). (B) Fin ray bases (see Fig. 4) allow fin rays of different stiffness to be attached. Grooved slots allow the fin ray tendons to emerge from the body interior. (C) Detail of fin ray bases with fin rays attached. Tendons from each side emerge and are tied to the fin ray bases. (D) Tensioners located above the water level allow fine adjustment of the tension in each fin ray tendon. (E) Interior view of the body to show the Teflon rods that serve as bearings to alter the tendon direction by 90 deg (tendons are visible as the thin white polyethylene threads) from the entry angle into the body to the direction needed for fin ray attachment at the caudal peduncle.

resulted in some bending of rays so that the tail was not truly flat and plate-like, all rays were driven by the same motion program and the base of tail was a uniform (flat) shape from dorsal to ventral. Three of the other four motion programs used the same excursion amplitudes as the flat motion, whereas the rolling motion had differential fin ray amplitudes. The cupping, undulation and W motions were created by changing the phase relationships between the fin rays as described below. For these motions, maximum transformation in fin shape developed as the fin passed through the mid-sagittal plane. The motor trajectories were chosen such that the bases of the fin rays moved through a ±27 deg sweep. This sweep angle was an average determined from a 3-D analysis of steady swimming caudal fin kinematics of bluegill sunfish.

The cupping motion of the tail is frequently observed in live bluegill (Flammang and Lauder, 2008; Lauder and Drucker, 2002; Tytell, 2006), and is generated by having the dorsal- and ventral-most fin rays lead the tail beat (Fig. 3, cupping motion). This results in the center of the tail lagging behind during lateral motion and producing a cup-like shape of the tail surface. The cupping motion was symmetrical about the midline. The middle fin rays lagged the dorsal and ventral fin rays by 25 and 50 deg (out of a 360 deg cycle).

The W-shape motion was produced when the two middle caudal fin rays, in addition to the dorsal- and ventral-most rays, led the tail beat. This generated a W-shape of the tail trailing edge (best seen in posterior view) with separate cupping areas in both the dorsal and ventral lobes of the fin (Fig. 3, W motion). This motion, which was symmetrical about the midline, applied phases of 0, –33 and –5 deg, to fin rays FR1, FR2 and FR3, respectively, in the dorsal tail lobe, and corresponding phases in the ventral lobe.

The undulation motion was generated by a dorsoventral phase-displaced wave of activation of the fin rays through the tail beat, producing a wave of bending that travels down the fin from dorsal to ventral, a direction orthogonal to the flapping motion (Fig. 3, undulation motion). For the undulation motion, phases of 0, –15, –30, –50, –65 and –75 deg, from the dorsal-most fin ray to the ventral-most fin ray, were applied.

Finally, the rolling motion was produced by having the fin rays undergo differential excursions so that there was a smooth reduction in excursion amplitude from dorsal to ventral among the six fin rays (Fig. 3, rolling motion). Ventral fin rays thus underwent much smaller side-to-side excursions than the upper fin rays, in contrast to the other four motion programs where all six fin rays moved through the same excursion, while preserving a zero phase lag. During this motion, the sweep of the fin rays decreased linearly from the dorsal-most fin ray to the ventral-most fin ray, with a maximum sweep of ±27 deg and a minimum of ±5 deg.

Mechanical properties of fin rays

The flexural rigidities – the modulus of elasticity (E) times the area moment of inertia (I) (Gere, 2004) – of the bluegill sunfish fin rays were determined by conducting three point bending test on freshly dissected fin rays. Methods for these tests are provided in Alben et al. (Alben et al., 2007) and Lauder et al. (Lauder et al., 2011a; Lauder et al., 2011b). Several points along the length of each caudal fin ray were tested by measuring the applied force and the resulting displacements. First-order Euler–Bernoulli equations were applied to data acquired from the three point bending tests to determine the passive flexural rigidities along fin ray lengths. This calculation ignored small changes in the width of the fin-ray over the approximately 2 mm test area.

Computed microtomography (voxel dimensions: x=0.049 mm, y=0.049 mm, z=0.12 mm) scans of a bluegill sunfish caudal fin (Fig. 1C) were used to estimate I along the lengths of different caudal fin rays. Approximately every 1.5 mm along the length of the fin ray, the microtomography slices were examined and the bone structure was outlined. To distinguish the edge of the bone structure from collagenous material, a 5×5 convolute filter was applied to each slice of the scan. To calculate the I of the bones, the outlines were converted to binary and imported to a MATLAB program (v. 7.6.0.324 R2008a; The MathWorks, Inc., Natick, MA, USA). A custom MATLAB program was developed to determine the bending axis and calculate the second area moment of inertia.

The flexural rigidities for the robotic fin rays were set so that one scaling of flexural rigidity values would be expected to behave and bend in a fashion similar to the biological fin rays, and other values were set to be more and less stiff to allow for an exploration of the stiffness parameter space and to determine the effect of fin ray stiffness on locomotor forces. To estimate the appropriate scaling for the robotic fin rays, fin ray bending was modeled using first-order cantilever Bernoulli–Euler equations. This ignored the inertial response of the fin rays as the fin was accelerated. The hydrodynamic loading of the fin was determined from drag and added mass forces

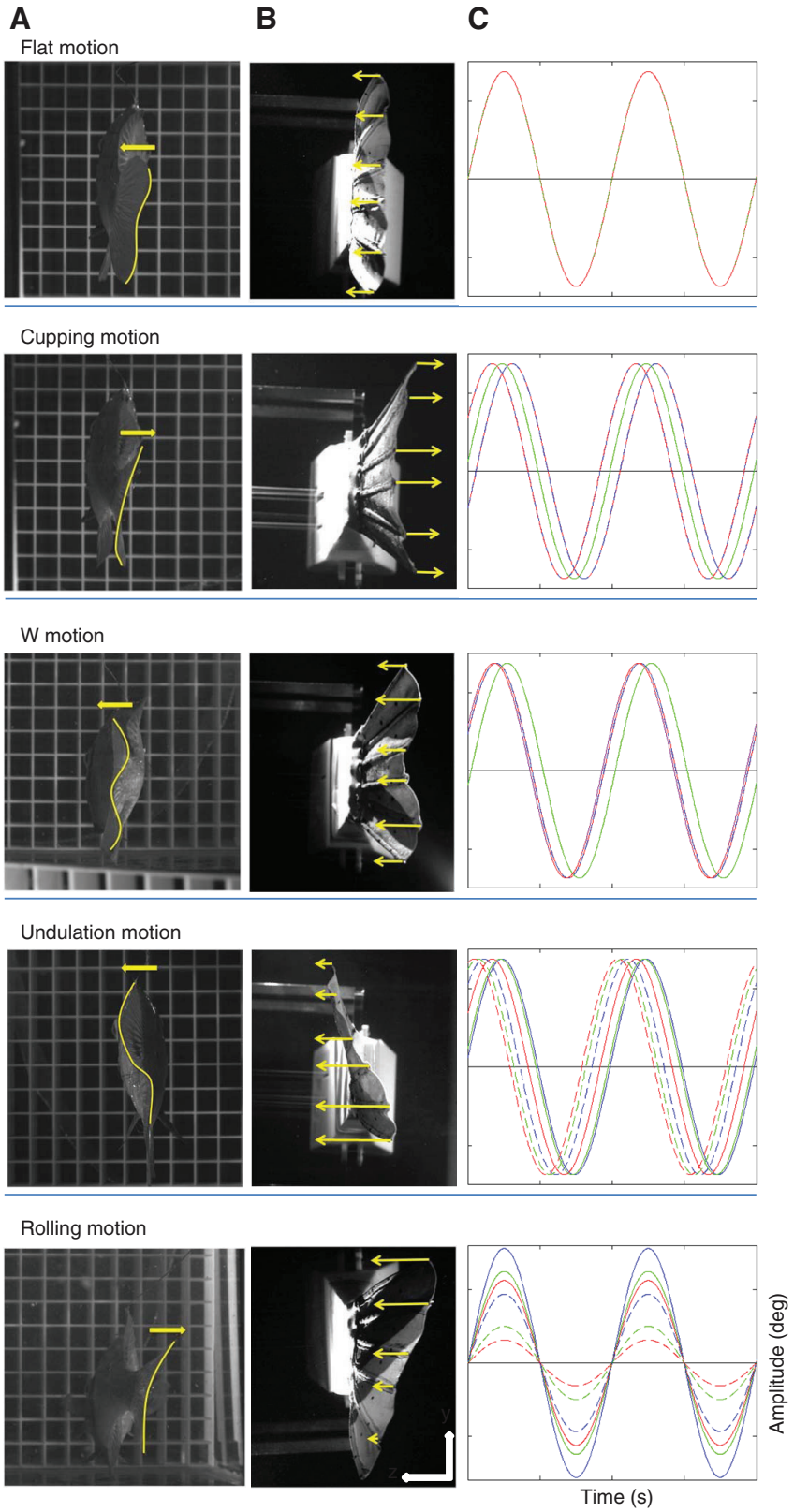

Fig. 3. Motion programs for the robotic caudal fin were based on observed sunfish caudal fin kinematics (see Lauder, 2000; Flammang and Lauder, 2008; Flammang and Lauder, 2009). (A) Posterior views of a bluegill sunfish performing steady swimming and maneuvering motions. (B) Posterior views of the robotic caudal fin performing similar caudal fin movements. Images of the robotic caudal fin were rotated 90 deg for comparison. Yellow arrows in A and B indicate the direction of motion of the individual fin rays. (C) The driven motion of the six robotic fin rays during two complete cycles (each fin ray motion is plotted in a different color and dash pattern); From top to bottom, fin ray 1 (blue solid), fin ray 2 (green solid), fin ray 3 (red solid), fin ray 4 (blue dash), fin ray 5 (green dash) and fin ray 6 (red dash).

applied to the fin webbing. The width of the fin webbing was assumed to increase linearly along the fin's length. As a result, the load from drag increased along the length of the fin with the square of the flapping frequency and with the cube of the distance from the peduncle. The load from the added mass increased along the length of the fin linearly with the fin's angular acceleration and with the fourth power of the fin's length. This assumed that each strip of the fin accelerated a volume of water that was equal to a section of a half cylinder with a diameter equal to the fin's width. A scaling factor of approximately 500× was estimated to be appropriate for robotic fins that had linear dimensions four times those of a biological fin and that were to be flapped between 0.5 and 2.0 Hz.

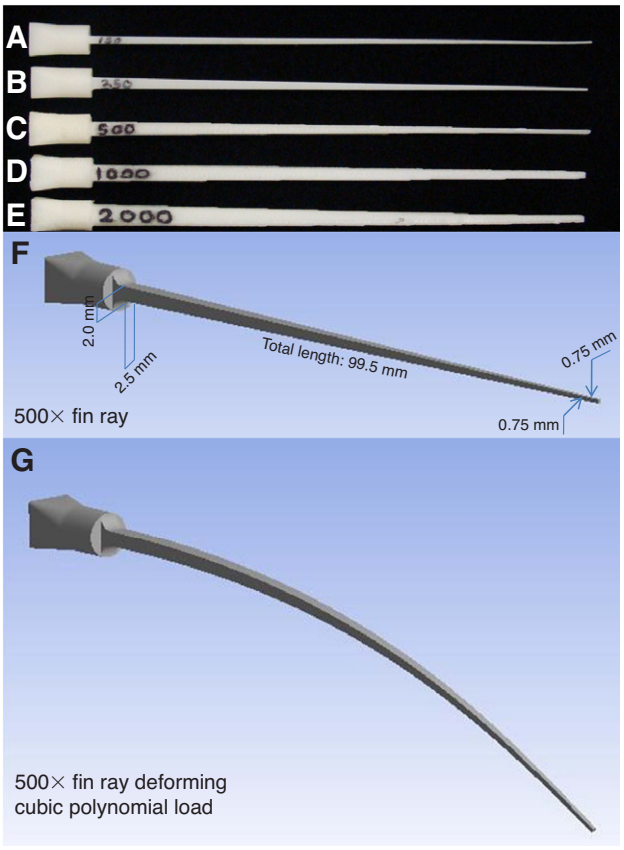

Fig. 4. Design of fin rays for the robotic caudal fin. (A–E) The scaled robotic fin rays taper in height and width along their length. Each of the fin rays is labeled with the corresponding scaled stiffness value. The base cross-sectional area and slope of the taper are changed to match the scaled flexural rigidity of the fish fin rays along their length. (F) Schematic of the 500× fin ray with no load applied to it. (G) A cubic polynomial load is applied, showing the bending curvature of the 500× fin ray.

The flexural rigidities of the biological fin rays were then multiplied by this scaling factor, and the cross-sectional geometries of the robotic fin rays were determined by fitting the flexural rigidities of the robotic fin rays to the scaled biological values. The robotic fin rays were tapered in both width and height along their lengths so that their bending characteristics approximated those of the biological fin rays as seen *in vivo* in previous 3-D kinematic studies of swimming bluegill sunfish (Figs 4, 5) (Flammang and Lauder, 2008; Flammang and Lauder, 2009).

Sets of robotic fin rays were manufactured with flexural rigidities 150 to 2000 times those of the biological fin rays (Fig. 4A–E). This range encompassed both very stiff (2000×) and very compliant (150×) fins. A further discussion of fin ray scaling to match the material properties of manufactured fin rays to those of the bluegill sunfish is given in Tangorra et al. (Tangorra et al., 2010). The fin rays were manufactured using fused deposition modeling (Stratasys Inc., Eden Prairie, MN, USA; material: ABS plastic) and stereolithography (3D Systems, Rock Hill, NC, USA; material: Accura 40 UV resin), and were approximately 10 cm long, excluding the attachment base (Fig. 4).

Experimentation

Experiments were conducted to determine how forces and flows were affected by alterations in fin ray stiffness, kinematic patterns and fin-beat frequency. Five fins with flexural rigidities scaled 150, 250, 500, 1000 and 2000 times the flexural rigidities of the biological fin rays were tested. For each of the five stiffnesses, five motions were tested: flat, undulation, cupping, W and rolling. The fin was actuated at frequencies of 0.5, 1.0, 1.5, 1.8, 2.0, 2.2 and 2.4 Hz. The fin was mounted above a recirculating flow tank used for previous experiments on both live bluegill and robotic pectoral fins (Lauder et al., 2007; Flammang and Lauder, 2008; Flammang and Lauder, 2009; Tangorra et al., 2009; Tangorra et al., 2010), and a flow speed of 100 mm s^{-1} was used for all tests.

The robotic caudal fin was suspended in the flow tank (Fig. 1E) from a low-friction air-bearing system mounted above the tank. This allowed the assembly to be attached to two force transducers that measure forces in the horizontal plane (for details, see Lauder et al., 2007; Tangorra et al., 2010; Lauder et al., 2011a). The robotic fin was oriented horizontally (Fig. 1), as if a fish was lying on its side. The forces measured in the horizontal plane, therefore, equated to thrust (along the rostrocaudal *x*-axis) and lift (along the dorsoventral axis, which we will refer to as the *y*-axis, as in the same orientation for a live, swimming fish).

The forces generated by the robotic caudal fin were measured using two Futek LSB200 S-beam load cells (44.5 N, LSB200, Futek Inc., Irvine, CA, USA) and sampled at 200 Hz (6036E data acquisition card, National Instruments, Austin, TX, USA). Data were processed using a low-pass filter to reduce noise. The filter used a Kaiser window with a passband frequency of 10 Hz, a stopband frequency of 12 Hz and a peak error of 10^{-3} (Oppenheim et al., 1989).

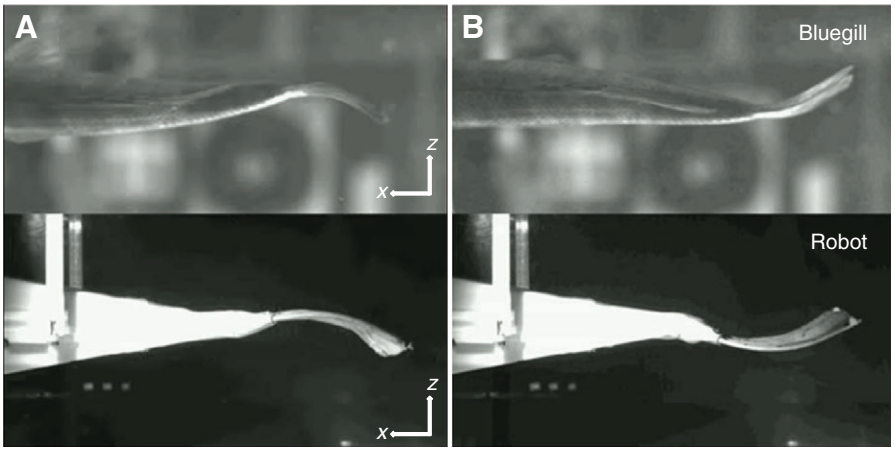

Fig. 5. Images from high-speed video to show the comparison between the motion of the bluegill sunfish caudal fin (upper) and that of the robotic caudal fin (lower) discussed in this paper. Two representative times are shown 180 deg out of phase to illustrate caudal fin deformation during locomotion. The robotic caudal fin is driven with a stiff body, in contrast to the deforming bluegill body, and robotic fin rays are actuated at joints with the caudal peduncle. Images have been scaled to the same approximate size; the actual length of the robotic tail is four times that of the bluegill tail. Similar curvatures between the robotic caudal fin and the bluegill tail are achieved with a scaled fin ray stiffness of 150× shown here. See supplementary material Movie 1.

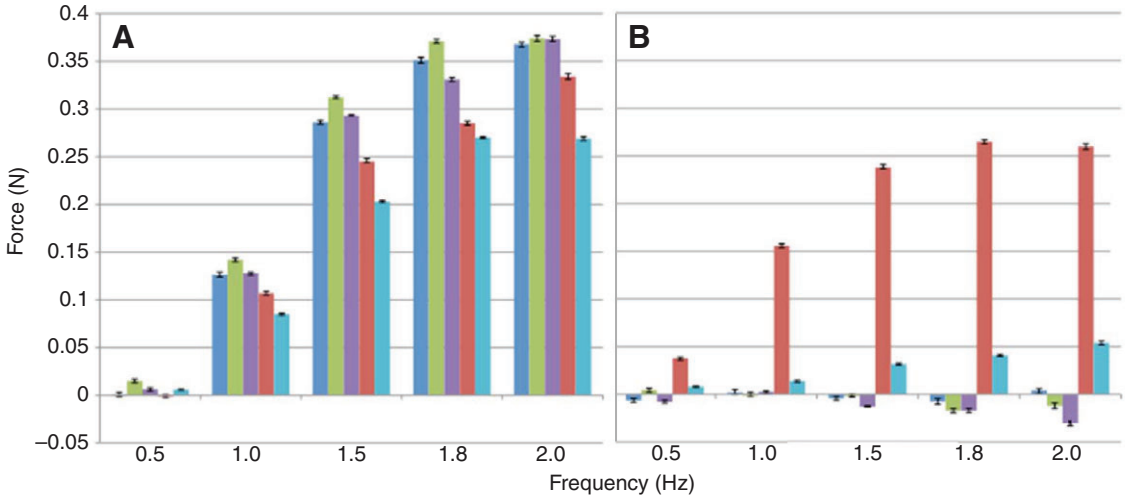

Fig. 6. Mean (A) thrust and (B) lift produced by the 1000× fin as flapping frequency was changed. Forces are shown for the flat (dark blue), cupping (green), W (purple), undulation (red) and rolling (light blue) motions. Means are based on five consecutive cycles and error bars represent ±1 s.d.

Force cycles for analysis were calculated by overlaying and averaging five consecutive stroke cycles. To reduce transients that are associated with startup, the first five fin-beat cycles were discarded. The collection and analysis process of the force measurements is further discussed in Tangorra et al. (Tangorra et al., 2010), as the procedures in the present study followed closely those used for our previous experiments on robotic pectoral fins. Critical values for differences in thrust production were determined through binomial tests (Zar, 1999).

Three high-speed (500 Hz), high-resolution (1 megapixel) cameras (Photron Fastcam PCI-1024 USA, Inc., San Diego, CA, USA) were positioned to capture the dorsal, lateral and posterior views of the fish and robot in the flow tank simultaneously with the force measurements, as in our previous research (Drucker and Lauder, 2005; Lauder et al., 2007; Lauder and Madden, 2007; Standen and Lauder, 2005; Standen and Lauder, 2007; Tangorra et al., 2010). These data provided 3-D kinematic views of the moving caudal fin, and calibration by direct linear transformation (Hedrick, 2008) allowed quantification of robotic caudal fin motion and *in vivo* fin ray bending.

Hydrodynamic wakes of the robotic caudal fin were studied using digital particle image velocimetry (DPIV), as in previous research (Drucker and Lauder, 1999; Lauder, 2000; Nauen and Lauder, 2002; Tangorra et al., 2010). Briefly, light from a continuous 8 W argon-ion laser was focused onto a light sheet that was projected (in separate experiments) both parallel to the plane of the tail and orthogonal to the tail plane. This allowed us to capture images of wake flow patterns generated by the robotic fin for comparison with those produced from freely swimming bluegill sunfish in previous experiments (Tongorra et al., 2010). DPIV data were collected simultaneously with force measurements.

RESULTS

Effects of changing the fin motion pattern

The force patterns generated by the robotic caudal fin are separated into two motion program groups – symmetrical and asymmetrical – to better explain how force is associated with fin motions. Forces from the symmetrical motions (flat, cupping and W) were primarily in the thrust direction, whereas forces from the asymmetrical motions (undulation and rolling) had both significant lift and thrust components (Fig. 6). Values reported below are means ± 1 s.d.

Forces from the symmetrical motions

The forces from the three symmetrical motions – flat, cupping and W – were primarily in the thrust direction. Although lift was produced, the magnitude of lift was very small. In all symmetrical cases, the average magnitude of the lift force over a cycle was less than 4% of the average magnitude of the thrust. In general, as the fin accelerated, fluid was pushed along the rostrocaudal axis of the fin and thrust forces developed with the fin's angular velocity. The magnitude of the thrust increased as the fin accelerated from its extreme lateral position towards the midline, with a peak being reached approximately when the fin reached mid-stroke (Fig. 7A). The timing of the maximum peak was dependent on fin stiffness and the actuation mode, but in all trials, the peak thrust force occurred approximately when the base of the fin passed through the midline. Often, small dips in the thrust force occurred before the maximum peak thrust force was reached (Fig. 7A). Thrust began to gradually decrease after the base of the fin reached its maximum velocity, which was when it passed through the midline. As the fin reversed direction, the gradual decrease in thrust turned into a net drag force (seen where the red curve dips below the zero force line in Fig. 7A). These results were consistent with previous results from studies that used computational fluid dynamics (CFD) to predict the forces generated by flexible, trapezoidal foils (Akhtar et al., 2007; Zhu and Shoele, 2008).

Although the force profiles created by the cupping motion were similar to those produced by the flat motion, the subtle changes that were made to the fin ray motions resulted in slight, but consistent, differences to the force profile. The differences between the magnitudes of the mean thrust forces were most pronounced when the fin was flapped at lower flapping frequencies and had higher fin stiffnesses; consequently, when there was little bending of the fin rays the conformations of the cupping and flat fins were most different. For example, when the fin was flapped at 1.0 Hz with a fin stiffness of 2000×, the flat, cupping and W motions produced magnitudes of mean thrust of 0.190±0.001, 0.203±0.001 and 0.198±0.001 N, respectively. This is a 7% difference between the flat and cupping, a 4% difference between the flat and W and a 3% difference between the cupping and W motion. When the fin used very compliant fin rays (150× and 250×) and/or the flapping frequency was high (1.8 Hz and 2.0 Hz), the forces produced by the

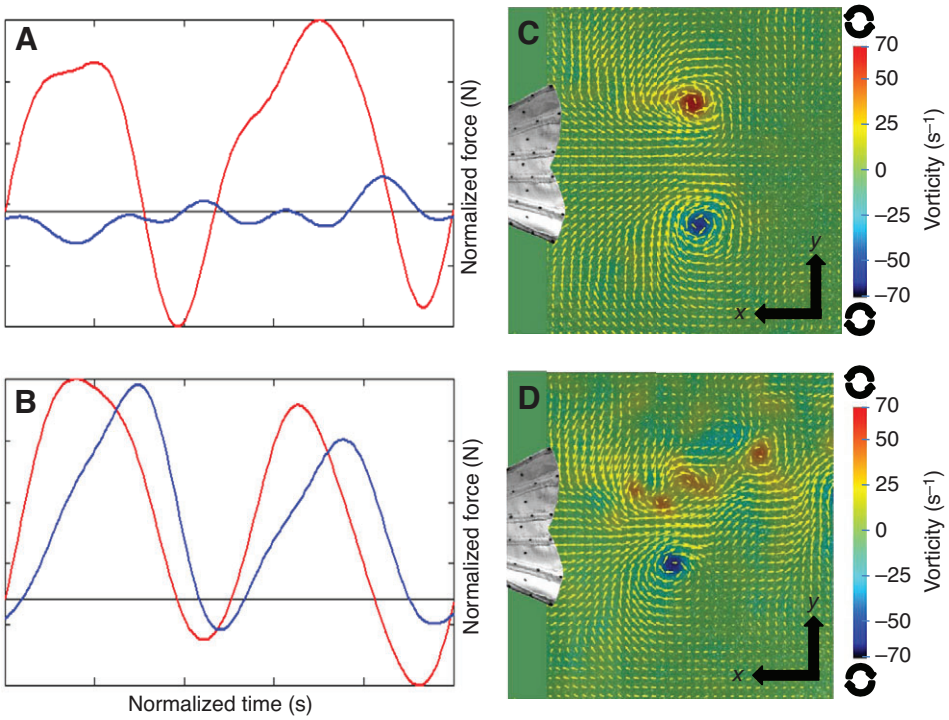

Fig. 7. (A,B) Normalized force traces and (C,D) digital particle image velocimetry (DPIV) images of associated wake flows, during one cycle, for the flat (A,C) and undulation (B,D) motions of the robotic caudal fin. In the force traces, the red line indicates the thrust force and the blue line indicates the lift force. The graphs have been normalized to show the pattern produced by the motion. In the flow images, red represents a positive (counterclockwise) rotation of fluid and blue/purple represents a negative (clockwise) rotation of fluid. Yellow arrows indicate the velocity and direction of the fluid. The green region indicates an area of zero vorticity. The free-stream flow is moving at 100 mm s^{-1} in the positive *x*-direction.

robotic caudal fin varied much less. At a flapping frequency of 1.8 Hz and a fin stiffness of 150×, the W and flat motions produced mean thrust forces of nearly the same magnitude. The cupping motion produced a magnitude mean thrust force that was 5% greater than that of the flat and W motions.

The mean forces created by the W motion were not significantly different than the forces created by the flat motion when the fin flexibility was low (150× and 250×; $P<0.05$) and/or when flapping frequency was high (1.8 Hz and 2.0 Hz; $P<0.05$). The forces were consistently greater when fin ray stiffness was increased and/or flapping frequency was decreased. These results are a function of multiple driving inputs and will be discussed in detail in later sections.

The mean thrust forces generated by the cupping motion were larger than those generated by both the symmetrical and asymmetrical motions during 84% (21 out of 25; $P<0.001$) of comparable trials. The cupping motion generated mean thrust forces that were 14±6% larger than those generated by the flat motion during comparable trials (Fig. 6). The cupping motion also produced mean thrust forces that were 8±3, 22±11 and 50±12% larger than those of the W, undulation and rolling motions. The three exceptions to this occurred during the W motion at a fin stiffness of 150× and a flapping frequency of 2.0 Hz, and the W motion with a fin stiffness of 500× and a flapping frequency of 1.8 and 2.0 Hz. In these three cases, the average magnitude of the thrust force produced by the W motion was less than 4% higher than that of the cupping motion.

Forces from the asymmetrical motions

In contrast to the small mean lift forces created by the symmetric motion programs, the asymmetric motions created lift and thrust forces where lift was of the same magnitude as thrust (Fig. 6). The thrust force profiles generated by the asymmetrical motions had a similar pattern to those of the flat motion (Fig. 7B). These results are consistent with those found by Lauder (Lauder, 2000), who identified that the asymmetrical motions created by the bluegill sunfish during steady swimming show both a thrust and a lift force during steady swimming. The undulation motion generated thrust force as the dorsal-most fin ray was accelerated from the extreme lateral position towards the midline (Fig. 7B). This thrust force gradually decreased and became a net drag force (Fig. 7B, where the red line dips below the zero line) once the ventral-most fin ray passed the midline and the dorsal-most fin ray began its reversal. Lift forces were generated when all the fin rays moved in the same direction, from one extreme lateral position to the other. There was a gradual decrease in lift force when the dorsal-most fin ray reversed its direction. This gradual decrease led to small negative lift forces being generated during the reversal period (Fig. 7B, where the blue line dips below the zero line). Lift forces were generated again when all the fin rays began moving in the same direction, after the reversal of the last (ventral-most) fin ray. The phase difference between the thrust and lift peak magnitudes was on average 38±4 deg. The variance is due to the bending of the fin rays.

The undulation motion generated lift forces that were of the same magnitude as the thrust forces and had two-dimensional force vectors that were, on average, larger than those created by all other motions. At flapping frequencies above 0.5 Hz, lift forces generated by the undulation motion were on average 27±3% lower than the thrust forces. At a flapping frequency of 0.5 Hz, the lift forces were significantly larger than the thrust forces. The magnitude of the mean thrust force generated by the undulation motion was on average 24±10% smaller than the magnitude of the mean thrust force generated by the flat motion. On average, the two-dimensional magnitudes of the undulation force were 48±6% higher than all other motions (48±1, 41±1 and 52±1% higher than the flat, cupping and W motions, respectively).

The rolling motion generated thrust force during the part of the sweep when the fin rays accelerated towards the midline from the extreme lateral position. After the fin passed the midline, the fin rays began to decelerate and to produce less thrust force. During a portion of the stroke between the point when the fin passed the midline and when the fin reversed its stroke, the thrust turned into a net drag force. Lift was created during the rolling motions when

the fin rays accelerated from the midline to the extreme lateral position. Negative lift was produced during the part of the sweep when the fin accelerated from the lateral-most position to the midline. The peak lift force occurred after the thrust peaks with an average phase difference of 155±5 deg.

The rolling motion generated thrust forces that were the smallest of all the symmetrical and asymmetrical motions, and mean lift forces that were only slightly positive. Lift forces during the stroke were only slightly larger than the negative lift forces generated, which caused the mean magnitude of lift to be only slightly positive. Thrust forces generated were of the same magnitude as those of the flat motion. Lift forces produced during the rolling motion had both large negative and positive magnitudes (–0.49 and 0.62 N, respectively) This caused the mean lift force to never be higher than 0.054±0.002 N, which was only 0.016 N larger than the smallest mean lift force generated by the undulation motion. The mean thrust forces generated by the rolling motion were on average 28±12% smaller than those generated by the flat motion and 21±7% smaller than those produced by the undulation motion.

Wake flows

The five robotic motions each produced different wake flows. The subtle kinematic differences between the three midline symmetrical motions resulted in only slightly different wake flows. The large differences in amplitude and phase between the asymmetrical motions resulted in significantly different wake flows.

The flat motion shed two tip vortices from the leading edges of the dorsal- and ventral-most fin rays (Fig. 7C). These vortices were counter-rotating and had approximately equal vorticity. The region between the vortices had an accelerated jet of fluid that was directed away from the robot along the midline.

The cupping motion produced two tip vortices that were similar to those generated by the flat motion. The vortices formed at the leading edges of the dorsal and ventral-most areas of the fin were also counter-rotating, and had approximately equal vorticity. The paths that the vortices translated along, however, were not parallel to the midline like the vortices shed by the flat motion. The cupping motion vortices were funneled inward towards the midline. This funneling caused an increase in fluid velocity between the vortices.

The W motion shed four vortices as the fin passed the midline and through the DPIV viewing area. Two of the vortices developed along the leading edges of the dorsal- and ventral-most fin rays. These vortices were similar in size and structure to those created by the other symmetrical motions. Similar to the wake vortices generated by the cupping motion, the vortices were funneled inward towards the midline. Two other vortices developed along the leading edge area around the notch of the fin. These vortices were equal to each other in size and structure, but were smaller and had lower vorticity than the vortices that developed along the dorsal- and ventral-most fin rays. The vortices that developed at the notch area were also funneled inwards as they translated away from the fin. The area between the four vortices had an accelerated jet of fluid directed away from the robot along the midline.

The undulation and rolling motions produced wake vortices that were asymmetrical about the midline and significantly more complex than the symmetrical motions. Both the asymmetrical motions shed multiple vortices throughout the stroke. The undulation motion produced wake flows that translated along the midline in the positive lift direction. A total of four vortices were created: two developed from the leading edge at the dorsal and ventral-most fin rays and two were created from the notch area (Fig. 7D). The two notch vortices were considerably smaller, had lower vorticity and translated at a quicker pace than the vortices created from the leading edge at the dorsal- and ventral-most fin rays. These notch vortices were consumed by the flow downstream because of their small size. The dorsal-most fin ray, FR 1, was the leading fin ray in the pattern. The first vortex was created when the leading edge of the dorsal-most fin ray passed through the viewing area. This vortex translated at an angle of approximately 25 deg off the midline in the lift direction (ventrally). The second set of vortices was created when the ventral-most fin ray, FR 6, passed through the viewing area. These vortices funneled towards the midline at a smaller angle than the dorsal vortex. These caused the area of accelerated fluid between these vortices to be directed in the lift direction (ventrally).

The rolling motion generated three noticeable vortices: one from the dorsal lobe, one from the ventral lobe and one from the notch area. Each of the three vortices was of different size and had different vorticity. The notch vortex was considerably smaller, had a lower vorticity and was quickly consumed by the flow downstream. The leading edge of the dorsal lobe shed the first vortex. Because the dorsal-most fin ray had the largest displacement, the dorsal lobe vortex was the largest. This vortex translated along the direction of the flow, funneling towards the midline. The vortex from the ventral lobe of the caudal fin was the second largest vortex and the third to be shed. The ventral lobe vortex translated at an angle towards the midline. Further downstream, the ventral vortex interacted with the notch and the dorsal vortex. The area of accelerated flow between the vortices was directed simultaneously along two paths, approximately ±45 deg off the midline.

Effects of altering fin ray stiffness

The forces generated by the robotic fin during the symmetrical and asymmetrical motions changed as the stiffness of the fin was altered (Fig. 8). The forces generated by each of the motions were affected differently by the stiffness of the fin, but general trends were apparent. The more compliant fins (150× and 250×) produced lower peak magnitude forces than the stiffer fins (1000× and 2000×). For example, during the flat motion at 1.5 Hz, the 150× fin produced a peak thrust force with a magnitude of 0.391±0.010 N. During the same conditions, the 2000× fin produced a peak thrust force with a magnitude of 0.594±0.013 N (52±3% larger).

The magnitudes of the peak and mean forces generated by the W motion were significantly affected by the stiffness of the fin and the flapping frequency. The magnitude of the peak and mean thrust forces generated by the W motion at low fin stiffness and/or high flapping frequency were similar to the forces generated by the flat motion. As stiffness was increased and/or flapping frequency was lowered, the difference between the forces was more pronounced. At a fin stiffness of 150× and a flapping frequency of 1.5 Hz, the mean thrust produced from the W motion was, on average, the same as that produced from the flat motion. As the stiffness of the fin increased, the magnitude of the mean thrust force created by the W motion increased at a faster rate than the flat motion. At a fin stiffness of 2000× and a flapping frequency of 1.5 Hz, the W motion produced, on average, 15±4% more mean thrust than the flat motion.

The mean thrust forces generated by the asymmetric and symmetric motion programs peaked at different fin stiffnesses, but on average, the largest mean thrust forces were produced by the 500× fin. During 80% (20 out of 25; $P<0.001$) of comparable experimental trials, the 500× fin produced the largest mean thrust forces. The 500× fin, during the flat motion, produced on average 64±9% more mean thrust than the 150× fin, 26±7% more mean thrust than the 250× fin, 15±7% more mean thrust than the 1000× fin and 18±8% more mean thrust than the 2000× fin. These results

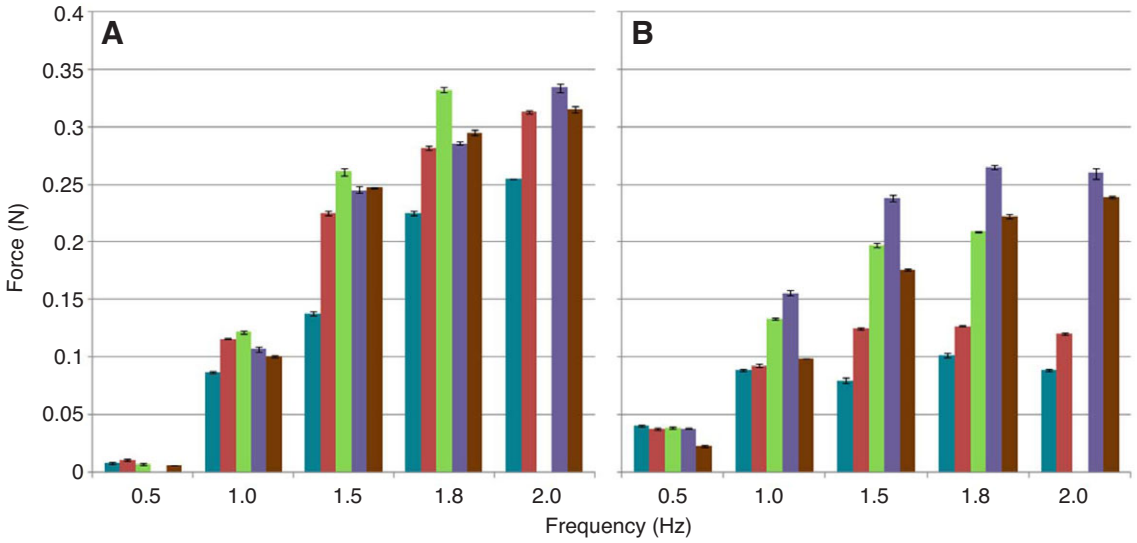

Fig. 8. Mean (A) thrust (B) and lift forces generated by the undulation motion by 150× (blue), 250× (red), 500× (green), 1000× (purple) and 2000× (brown) stiffness fin rays. Bars are grouped by frequency. Means are based on five consecutive cycles and error bars at the peaks represent ±1 s.d. associated with each stiffness.

are representative of the other motions; the exact percent differences in mean thrust force depended on multiple factors, but the trend was common for all the robotic caudal fin motions. Out of the five experimental trials where the 500× fin did not produce the largest magnitude mean thrust, four were at a flapping frequency of 0.5 Hz. The last exception was the W motion at a flapping frequency of 1.8 Hz. The 1000× fin produced, on average, 1±4% more force than the 500× fin.

The mean lift forces produced by the robotic caudal fin during the asymmetrical motions – undulation and rolling – peaked at a particular stiffness (Fig. 8). The 1000× fin, when actuated through the asymmetrical motions, produced the largest magnitude mean lift forces during 75% of comparable trials (six out of eight; $P>0.05$). On average, the 1000× fin produced magnitude mean lift forces that were 123±54% larger than the very compliant 150× fin, 16±4% larger than the 500× fin and 37±21% larger than the very stiff 2000× fin. The two exceptions happened at the 0.5 Hz flapping frequency during both the undulation and rolling motions. At this low flapping frequency, the 150× fin produced the largest mean lift force, which was only 7% (0.003 N) higher than the 1000× fin.

Effects of changing flapping frequency

As expected, when the flapping frequency of the robotic fin was increased, the magnitudes of the forces generated during the five motions also increased. This trend held for all comparable experiment trails. The robotic caudal fin performing the flat motion with a fin stiffness of 1000× generated mean thrust forces that are representative of the overall trend. With an increase in flapping frequency from 1.0 to 1.5 Hz, the mean thrust increased by 227%. An increase in the flapping frequency by an equal amount, from 1.5 to 2.0 Hz, increased the mean thrust by only 128%. At higher flapping frequencies, the mean thrust force increased at a slower rate than at lower flapping frequencies. The exact increases in mean thrust force depended on the stiffness of the fin, the driven motion of the fin rays and the increase in flapping frequency, but the trend was common for all the robot caudal fin motions and stiffnesses.

The peak magnitude and mean forces generated by the W motion were significantly affected by alterations in the stiffness and the flapping frequency of the fin. As previously shown, the W motion produced on average the same force as the flat motion at low fin ray stiffnesses. As the stiffness of the fin rays increased, the mean thrust force created by the W motion increased at a faster rate than that created by the flat motion. A similar result was also found if the fin stiffness was held constant and the flapping frequency was increased. At a fin stiffness of 250× and a flapping frequency of 1.0 Hz, the W motion outperformed the flat motion by 5±1%. When the flapping frequency was increased from 1.0 to 2.0 Hz and the fin stiffness was held constant at 250×, the W and flat motions produced on average the same mean thrust force.

During both the rolling and undulation motions, the magnitude of the mean lift forces peaked depending on the stiffness and flapping frequency. With a fin stiffness of 1000×, the mean lift forces created by the undulation and rolling motions peaked at 1.8 Hz. At flapping frequencies higher than 1.8 Hz, the mean lift forces produced by the fin decreased. The more compliant fins (150×, 250× and 500×) peaked at slightly lower flapping frequencies (1.5–1.8 Hz). The stiffer fin (2000×) peaked at slightly higher flapping frequency (2.0 Hz).

DISCUSSION

Robotic and biological caudal fins

The robotic caudal fin was designed to allow for the production of a variety of motions that had been observed in previous studies of bluegill sunfish caudal fin during locomotion and maneuvering (Lauder, 2000; Flammang and Lauder, 2008; Flammang and Lauder, 2009). By designing the fin with individually controllable fin rays that could be varied in stiffness among experiments, we were able to assess the effect of tail fin ray stiffness on locomotor performance, and to manipulate the motion program and to quantify patterns of thrust and lift force generation with changes in tail-beat frequency. Although previous functional studies of caudal fin locomotion in freely swimming fishes have been instrumental in contributing to our understanding of aquatic propulsion, the inability to manipulate and isolate key biomechanical parameters has hindered our understanding of fundamental properties relevant to caudal propulsion, such as stiffness and movement pattern. In addition,

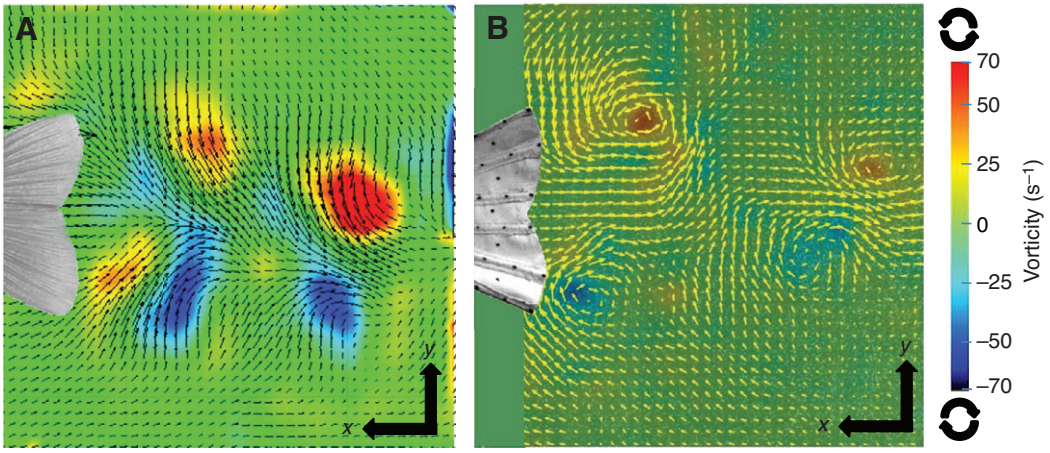

Fig. 9. DPIV images, from a lateral view, of (A) a bluegill sunfish and (B) the robotic caudal fin during rolling tail motion. The fish caudal fin and the robotic caudal fin have been superimposed to show their position relative to the flow. In the flow images, yellow/red represents a positive (counterclockwise) rotation of fluid, whereas blue/purple represents a negative (clockwise) rotation of fluid. Yellow and black arrows indicate the velocity and direction of the fluid. For both images, the green regions indicate an area of zero vorticity. The flow is moving in the positive *x*-direction.

measuring forces from freely swimming fishes is challenging and subject to a number of assumptions that make interpreting these data difficult (Dabiri, 2005; Drucker and Lauder, 1999; Peng and Dabiri, 2008; Peng et al., 2007). In contrast, quantifying time-dependent patterns of thrust and lift force production in a robotic device is more manageable and allows the effect of changing fin ray stiffness, frequency and motion program on locomotor performance to be relatively easily assessed.

Using an approach that investigated and modeled the caudal fin kinematics of bluegill sunfish, we developed a robotic device that was able to effectively perform biologically relevant motions and generate wake flows that were similar to those of a live fish (Figs 5, 9). Appropriate scaling of fin ray flexural rigidities and the careful kinematic and hydrodynamic analysis of live fish were key to creating a robotic model that performed in a biologically relevant manner.

The robotic caudal fin exhibited a number of properties that are similar to those of the bluegill sunfish tail fin. Comparison of the fin ray curvatures and tip deflections exhibited by the robotic fin rays showed that both the curvature values and relative tip deflections were similar to those of the biological fin rays during the prescribed motions. As previously noted, the flexural rigidities of the robotic fin rays and fish scaled equivalently along their lengths. When the results from tracking the bending curvature and tip deflection of the biological and robotic fin rays were reviewed, it was noticed that fin rays of certain stiffness performed better than others at particular frequencies. The 500×, 250× and 150× robotic fins driven at frequencies between 1.5 and 2.0 Hz resulted in tip deflection and bending curvature similar to that of the bluegill sunfish. Further examination found that flapping the 150× at 1.5 Hz produced curvatures and tip deflections most comparable to those the sunfish. At higher stiffnesses, 1000× and 2000×, the fin lacked significant curvature, due to the stiff flexural rigidities and the frequency range tested.

Furthermore, the wake flows created by the robotic caudal fin were similar to the wake patterns created by the bluegill sunfish caudal fin. Both the bluegill caudal fin and the robotic tail generated two tip vortices as the fin passed throughout the viewing area (Fig. 9). These vortices are counter-rotating and of similar vorticity. During the asymmetrical robotic motions, the vortices translated along a path on the positive *y*-axis (dorsoventral axis) and positive *x*-axis (rostrocaudal axis). During the cupping and W motions, the tip vortices were funneled inwards as they translated along the *y*-axis (dorsoventral axis) (Fig. 6A). This funneling effect can also be seen during *in vivo* bluegill locomotion (Flammang et al., 2011; Lauder, 2000; Lauder, 2006; Lauder and Madden, 2006). Components of the vortex structure created from the steady swimming motion of the bluegill sunfish also proved to be similar to those created by the robotic fin during all five motions.

Effect of fin motion and shape on forces and flows

Altering the motion of the fin rays, through either phase or amplitude changes, varied the forces and flows that were generated by the caudal fin robot. Using the flat motion as a control, large variations in the fin motion, such as asymmetrical motions, caused large changes in forces and flow pattern. Small variations in fin motion, such as the phase changes associated with the symmetrical motions, caused smaller changes in the force profiles. These results were consistent with those found by Zhu and Shoele (Zhu and Shoele, 2008) using CFD to predict the forces generated by flexible, trapezoidal foils.

The forces and wake flows produced by the symmetrical motions were similar, but the subtle changes that were made to the fin ray motions resulted in slight, but consistent, differences. The cupping motion was able to produce significantly more thrust than the other symmetrical motions. These results are constant with previous CFD analysis that has shown that basic cupping motion might offer greater thrust production for flapping foils (Liu and Bose, 1997). In addition, the cupping motion of ray-finned fishes is a common mode of movement, and has been observed in the pectoral fins of several species. In bluegill sunfish, the kinematics of pectoral fin cupping have been described (Lauder et al., 2006; Lauder et al., 2007), as have fluid flows (both computed and measured) associated with steady swimming (Bozkurttas et al., 2009; Dong et al., 2010; Mittal et al., 2006). In pectoral fins, cupping motion has been demonstrated to minimize lift forces that are generated by asymmetrical fin motions, and to increase thrust on the outstroke.

A cupping fin motion has been observed in the caudal fin of a bluegill sunfish during steady swimming (Flammang and Lauder, 2008; Tytell, 2006), but the functional significance of the cupping motion is not fully understood. The vortex structure of the cupping

motion may help explain why it was able to produce higher mean thrust than the flat motion. The cupping motion produced vortices that were similar to those produced by the flat motion, with the main difference being the path along which the vortices moved. The funneling motion of the vortices produced by the cupped fin caused an increase in fluidic velocity between the dorsal and ventral fin margins. These results suggested that the increase in fluidic velocity between the vortices may be the reason for the observed increase in thrust force (Fig. 6).

The larger variations in the flat motion – the asymmetrical motions – caused significant changes to the forces and flows generated by the robotic caudal fin. In particular, the undulation motion was able to produce mean thrust and lift forces of the same magnitude. The undulation motion also produced larger two-dimensional forces than all the other motions during all comparable trials. The undulation motion produced vortices that translated along a path at an angle off the midline directions. The vortices shed off the caudal fin of a bluegill sunfish during steady swimming followed a path that was similar to that of the vortices shed by the undulation motion. This vortex structure has been analyzed and has been shown to produce forces both in lift and thrust directions (Lauder, 2000). Because the components of the vortex structure of the undulation and the steady swimming motion of the bluegill sunfish were similar (Fig. 9), and the motion had similarities to the phased flapping motion shown in Lauder (Lauder, 2000), it would indicate that components of the force structure might also contain similarities in freely swimming fishes.

Effect of fin stiffness on forces and wake flows

Flexibility of the robotic caudal fin played an important role in force production. By testing multiple fin stiffnesses, it was determined that the magnitude of the mean thrust and lift forces peaked at particular flapping frequencies. This implies that there were optimal fin stiffnesses for different scenarios (flapping frequencies, fin shape and flow speeds). The 500× fin produced the largest mean thrust forces during a majority of the comparable experimental trials. During the asymmetrical motions, the 1000× fin produced the largest lift during a majority of the comparable experiments. These fin stiffnesses (500× and 1000×) were neither the most complaint nor the stiffest. These findings are consistent with previous research that has indicated that there are optimal stiffnesses in flapping foil motion (Lauder and Madden, 2006; Akhtar et al., 2007; Zhu and Shoele, 2008; Tangorra et al., 2010; Lauder et al., 2011a).

During the symmetrical motions, there were distinct relationships between the compliance of the fin and its ability to produce the driven motion at the fin tip. When the W motion produced similar mean and peak forces to that of the flat motion, it was apparent through high-speed video that the fin ray tip motions were very similar between the two swimming motions. The subtle variations of the symmetrical motions got lost in the extensive bending and twisting of the fin rays that occurred at lower fin stiffnesses (150× and 250×) and/or at high flapping frequencies (1.8 and 2.0 Hz). At higher stiffnesses and/or lower flapping frequencies, the W motion was able to produce larger thrust force than the flat motion. During these situations, through examination of high-speed video, the fin ray tips were producing a distinct W motion. It was clear, during the W motion, that when the fin ray tips produced a motion similar to their driven motion, the subtle phase changes of the motion produced greater force than the flat motion. When the W motions produced greater thrust than the flat motion, an increase in fluid velocity was seen between the vortices generated compared with the flat motion.

Effect of flapping frequency on forces and flows

Modulating the flapping frequency of the robotic caudal fin caused changes to thrust and lift forces produced. At lower flapping frequencies (0.5 Hz), the thrust forces produced by the fin were significantly smaller than those produced by the higher flapping frequencies (2.0 Hz). During the range tested, the thrust forces continued to increase as flapping frequencies increased, in contrast to the lift forces, which peaked at different flapping frequencies. Each of the different fin stiffnesses peaked at different flapping frequencies during the asymmetrical motions. The 1000× fin during undulation generated a mean lift peak force at 1.8 Hz; when driven at higher frequencies, 2.0, 2.2 and 2.4 Hz, lift production decreased. The 2000× during the same driving conditions peaked at a flapping frequency of 2.0 Hz.

At very low flapping frequencies (0.5 Hz) all of the fins except the 150× fin exhibited very little bending. During all of the motions, the magnitude of the mean thrust forces produced at 0.5 Hz flapping frequency were very similar for all the fin stiffnesses, except 150×. Examining the videos of the fin, it was evident that at this low flapping frequency, the 150× fin was the only one to exhibit significant bending. The small amount of bending that was seen during this trial (0.5 Hz and 150×) could be the reason why the 150× fin was able to produce slightly higher magnitude mean thrust forces.

The relationship between fin ray bending and force production is one area that future studies could explore in more detail. Fin ray flexibility is a noteworthy aspect of the swimming of many live fishes, and bending of the tail surface to produce complex deformations is likely to be an important aspect of how fish control the magnitude and direction of locomotor forces. And yet, comparative data on the magnitude and time course of fin ray deformation are scarce. A few studies on a limited number of species have quantified *in vivo* fin ray bending patterns and curvatures, but a more comprehensive data set on fin ray deformation from a diversity of fishes executing an array of locomotor behaviors would be very useful for the development of future robotic models.

ACKNOWLEDGEMENTS

We thank members of the Lauder and Tangorra laboratories for many helpful discussions on fish tail mechanics, and Alexander Stubbs for assistance with the fin ray bending tests.

FUNDING

This work was supported by Office of Naval Research [grant number N00014-09-1-0352] on fin neuromechanics monitored by Dr Thomas McKenna, and by National Science Foundation [EFRI-0938043 to M. Philen (PI), and J.L.T. and G.V.L. (co-PIs)].

REFERENCES

Akhtar, I., Mittal, R., Lauder, G. V. and Drucker, E. (2007). Hydrodynamics of a biologically inspired tandem flapping foil configuration. *Theor. Comp. Fluid Dyn.* **21**, 155-170.

Alben, S., Madden, P. G. A. and Lauder, G. V. (2007). The mechanics of active fin-shape control in ray-finned fishes. *J. R. Soc. Interf.* **4**, 243-256.

Alvarado, P. V. and Youcef-Toumi, K. (2006). Design of machines with compliant bodies for biomimetic locomotion in liquid environments. *J. Dyn. Syst. Meas. Control* **128**, 3.

Anton, M., Chen, Z., Kruusmaa, M. and Tan, X. (2009). Analytical and computational modeling of robotic fish propelled by soft actuation material-based active joints. In *Proceedings of the IEEE/RSJ International Conference on Intelligent Robots and Systems*, pp. 2126-2131.

Barrett, D., Triantafyllou, M., Yue, D., Grosenbaugh, M. and Wolfgang, M. (1999). Drag reduction in fish-like locomotion. *J. Fluid Mech.* **392**, 183-212.

Bozkurttas, M., Mital, R., Dong, H., Lauder, G. V. and Madden, P. (2009). Low-dimensional models and performance scaling of a highly deformable fish pectoral fin. *J. Fluid Mech.* **631**, 311-342.

Dabiri, J. O. (2005). On the estimation of swimming and flying forces from wake measurements. *J. Exp. Biol.* **208**, 3519-3532.

Dong, H., Bozkurttas, M., Mittal, R., Madden, P. and Lauder, G. V. (2010). Computational modelling and analysis of the hydrodynamics of a highly deformable fish pectoral fin. *J. Fluid Mech.* **645**, 345-373.
Drucker, E. G. and Lauder, G. V. (1999). Locomotor forces on a swimming fish: three-dimensional vortex wake dynamics quantified using digital particle image velocimetry. *J. Exp. Biol.* **202**, 2393-2412.
Drucker, E. G. and Lauder, G. V. (2005). Locomotor function of the dorsal fin in rainbow trout: kinematic patterns and hydrodynamic forces. *J. Exp. Biol.* **208**, 4479-4494.
Flammang, B. E. and Lauder, G. V. (2008). Speed-dependent intrinsic caudal fin muscle recruitment during steady swimming in bluegill sunfish, *Lepomis macrochirus*. *J. Exp. Biol.* **211**, 587-598.
Flammang, B. E. and Lauder, G. V. (2009). Caudal fin shape modulation and control during acceleration, braking and backing maneuvers in bluegill sunfish, *Lepomis macrochirus*. *J. Exp. Biol.* **212**, 277-286.
Flammang, B. E., Lauder, G. V., Troolin, D. R. and Strand, T. E. (2011). Volumetric imaging of fish locomotion. *Biol. Lett.* **7**, 695-698.
Gere, J. M. (2004). *Mechanics of Materials*. Belmont, CA: Thomson.
Hedrick, T. L. (2008). Software techniques for two- and three-dimensional kinematic measurements of biological and biomimetic systems. *Bioinspir. Biomim.* **3**, 034001-034006.
Lauder, G. V. (1982). Structure and function in the tail of the pumpkinseed sunfish (*Lepomis gibbosus*). *J. Zool.* **197**, 483-495.
Lauder, G. V. (2000). Function of the caudal fin during locomotion in fishes: kinematics, flow visualization, and evolutionary patterns. *Am. Zool.* **40**, 101-122.
Lauder, G. V. (2006). Locomotion. In *The Physiology of Fishes, Third Edition* (ed. D. H. Evans and J. B. Claiborne), pp. 3-46. Boca Raton, FL: CRC Press.
Lauder, G. V. and Drucker, E. G. (2002). Forces, fishes, and fluids: Hydrodynamic mechanisms of aquatic locomotion. *News Physiol. Sci.* **17**, 235-240.
Lauder, G. V. and Drucker, E. G. (2004). Morphology and experimental hydrodynamics of fish fin control surfaces. *IEEE J. Ocean. Eng.* **29**, 556-571.
Lauder, G. V. and Madden, P. G. A. (2006). Learning from fish: kinematics and experimental hydrodynamics for roboticists. *Int. J. Automat. Comp.* **4**, 325-335.
Lauder, G. V. and Madden, P. G. A. (2007). Fish locomotion: kinematics and hydrodynamics of flexible foil-like fins. *Exper. Fluids* **43**, 641-653.
Lauder, G. V., Madden, P. G. A., Mittal, R., Dong, H. and Bozkurttas, M. (2006). Locomotion with flexible propulsors: I. Experimental analysis of pectoral fin swimming in sunfish. *Bioinspir. Biomim.* **1**, S25-S34.
Lauder, G. V., Anderson, E. J., Tangorra, J. L. and Madden, P. G. A. (2007). Fish biorobotics: kinematics and hydrodynamics of self-propulsion. *J. Exp. Biol.* **210**, 2767-2780.
Lauder, G. V., Madden, P. G. A., Tangorra, J. L., Anderson, E. and Baker, T. V. (2011a). Bioinspiration from fish for smart material design and function. *Smart Mater. Struct.* **20,** 094014.
Lauder, G. V., Lim, J., Shelton, R., Witt, C., Anderson, E. J. and Tangorra, J. L. (2011b). Robotic models for studying undulatory locomotion in fishes. *Mar. Technol. Soc. J.* **45**, 41-55.
Liu, P. and Bose, N. (1997). Propulsive performance from oscillating propulsors with spanwise flexibility. *Proc. R. Soc. Lond. A* **453**, 1763-1770.
Long, J. H., Jr, Koob, T. J., Irving, K., Combie, K., Engel, V., Livingston, N., Lammert, A. and Schumacher, J. (2006). Biomimetic evolutionary analysis: testing the adaptive value of vertebrate tail stiffness in autonomous swimming robots. *J. Exp. Biol.* **209**, 4732-4746.
Long, J. H., Porter, M. E., Root, R. G. and Liew, C. W. (2010). Go reconfigure: how fish change shape as they swim and evolve. *Integr. Comp. Biol.* **50**, 1120-1139.
Low, K. H. and Chong, C. W. (2010). Parametric study of the swimming performance of a fish robot propelled by a flexible caudal fin. *Bioinspir. Biomim.* **5**, 046002.
Mittal, R., Dong, H., Bozkurttas, M., Lauder, G. V. and Madden, P. G. A. (2006). Locomotion with flexible propulsors: II. Computational modeling of pectoral fin swimming in sunfish. *Bioinspir. Biomim.* **2006**, S35-S41.
Nauen, J. C. and Lauder, G. V. (2002). Hydrodynamics of caudal fin locomotion by chub mackerel, *Scomber japonicus* (Scombridae). *J. Exp. Biol.* **205**, 1709-1724.
Oppenheim, A. V., Schafer, R. W. and Buck, J. R. (1989). Discrete-time signal processing. Englewood Cliffs, NJ: Prentice Hall.
Peng, J. and Dabiri, J. O. (2008). An overview of a Lagrangian method for analysis of animal wake dynamics. *J. Exp. Biol.* **211**, 280-287.
Peng, J., Dabiri, J. O., Madden, P. G. and Lauder, G. V. (2007). Non-invasive measurement of instantaneous forces during aquatic locomotion: a case study of the bluegill sunfish pectoral fin. *J. Exp. Biol.* **210**, 685-698.
Shoele, K. and Zhu, Q. (2009). Fluid-structure interactions of skeleton-reinforced fins: performance analysis of a paired fin in lift-based propulsion. *J. Exp. Biol.* **212**, 2679-2690.
Standen, E. M. and Lauder, G. V. (2005). Dorsal and anal fin function in bluegill sunfish *Lepomis macrochirus*: three-dimensional kinematics during propulsion and maneuvering. *J. Exp. Biol.* **208**, 2753-2763.
Standen, E. M. and Lauder, G. V. (2007). Hydrodynamic function of dorsal and anal fins in brook trout (*Salvelinus fontinalis*). *J. Exp. Biol.* **210**, 325-339.
Tangorra, J. L., Davidson, S. N., Hunter, I. W., Madden, P. G. A., Lauder, G. V., Dong, H., Bozkurttas, M. and Mittal, R. (2007). The development of a biologically inspired propulsor for unmanned underwater vehicles. *IEEE J. Ocean. Eng.* **32**, 533-550.
Tangorra, J. L., Esposito, C. J. and Lauder, G. V. (2009). Biorobotic fins for investigations of fish locomotion. In: *Proceedings of the IEEE/RSJ International Conference on Intelligent Robots and Systems*, pp. 2120-2125.
Tangorra, J. L., Lauder, G. V., Hunter, I. W., Mittal, R., Madden, P. G. A. and Bozkurttas, M. (2010). The effect of fin ray flexural rigidity on the propulsive forces generated by a biorobotic fish pectoral fin. *J. Exp. Biol.* **213**, 4043-4054.
Tytell, E. D. (2006). Median fin function in bluegill sunfish Lepomis macrochirus: streamwise vortex structure during steady swimming. *J. Exp. Biol.* **209**, 1516-1534.
Tytell, E. D., Standen, E. M. and Lauder, G. V. (2008). Escaping Flatland: three-dimensional kinematics and hydrodynamics of median fins in fishes. *J. Exp. Biol.* **211**, 187-195.
Zar, J. H. (1999). *Biostatistical Analysis*. Upper Saddle River, NJ: Prentice Hall.
Zhang, Y.-h., Song, Y., Yang, J. and Low, K. H. (2008). Numerical and experimental research on modular oscillating fin. *J. Bionic Eng.* **5**, 13-23.
Zhu, Q. and Shoele, K. (2008). Propulsion performance of a skeleton-strengthened fin. *J. Exp. Biol.* **211**, 2087-2100.